

## QUANTUM ELECTRONICS

# Probing Johnson noise and ballistic transport in normal metals with a single-spin qubit

S. Kolkowitz,<sup>1\*</sup> A. Safra,<sup>1\*</sup> A. A. High,<sup>1,2</sup> R. C. Devlin,<sup>2</sup> S. Choi,<sup>1</sup> Q. P. Unterreithmeier,<sup>1</sup> D. Patterson,<sup>1</sup> A. S. Zibrov,<sup>1</sup> V. E. Manucharyan,<sup>3</sup> H. Park,<sup>1,2†</sup> M. D. Lukin<sup>1†</sup>

Thermally induced electrical currents, known as Johnson noise, cause fluctuating electric and magnetic fields in proximity to a conductor. These fluctuations are intrinsically related to the conductivity of the metal. We use single-spin qubits associated with nitrogen-vacancy centers in diamond to probe Johnson noise in the vicinity of conductive silver films. Measurements of polycrystalline silver films over a range of distances (20 to 200 nanometers) and temperatures (10 to 300 kelvin) are consistent with the classically expected behavior of the magnetic fluctuations. However, we find that Johnson noise is markedly suppressed next to single-crystal films, indicative of a substantial deviation from Ohm's law at length scales below the electron mean free path. Our results are consistent with a generalized model that accounts for the ballistic motion of electrons in the metal, indicating that under the appropriate conditions, nearby electrodes may be used for controlling nanoscale optoelectronic, atomic, and solid-state quantum systems.

Understanding electron transport, dissipation, and fluctuations at submicrometer length scales is critical for the continued miniaturization of electronic (1, 2) and optical devices (3–5), as well as atom and ion traps (6–10), and for the electrical control of solid-state quantum circuits (11). Although it is well known that electronic transport in small samples defies the conventional wisdom associated with macroscopic devices, resistance-free transport is difficult to observe directly. Most of the measurements demonstrating these effects make use of ohmic contacts attached to submicrometer-scale samples and observe quantized but finite resistance corresponding to the voltage drop at the contact of such a system with a macroscopic conductor (12, 13). Techniques for noninvasive probing of electron transport are being actively explored (14, 15), because they can provide insights into electronic dynamics at small length scales. Our approach makes use of the electromagnetic fluctuations associated with Johnson noise close to a conducting surface, which can be directly linked to the dielectric function at similar length scales, providing a noninvasive probe of electronic transport inside the metal. Measurements of these fluctuations at micrometer length scales with cold, trapped atoms showed excellent agreement with predictions based on diffusive electron motion (7–9), whereas millimeter-length scale measurements with superconducting quantum interference devices (SQUIDs) have been demonstrated for use as an accurate, contact-free thermometer (16).

Our approach makes use of the electronic spin associated with nitrogen-vacancy (NV) defect centers in diamond to study the spectral,

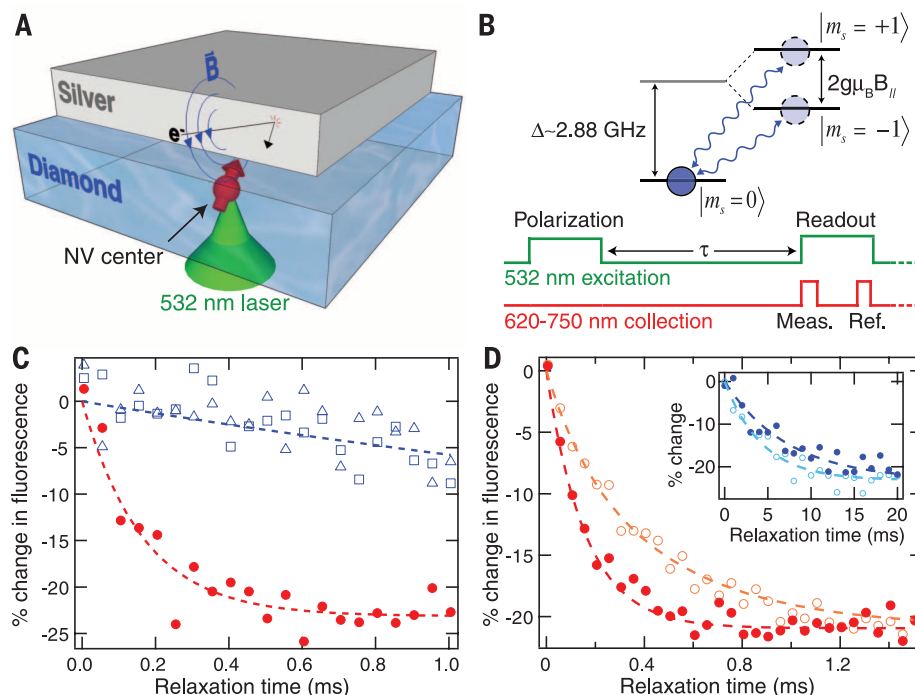


**Fig. 1. Probing Johnson noise with single-spin qubits.** (A) The thermally induced motion of electrons in silver generates fluctuating magnetic fields ( $\vec{B}$ ), which are detected with the spin of a single NV. The NV is polarized and read out through the back side of the diamond. (B) The NV spin is polarized into the  $|m_s = 0\rangle$  state using a green laser pulse. Spin relaxation into the  $|m_s = \pm 1\rangle$  states is induced by magnetic field noise at  $\sim 2.88$  GHz. After wait time  $\tau$ , the population left in  $|m_s = 0\rangle$  is read out by spin-dependent fluorescence. All measurements shown were performed at low magnetic fields ( $\Delta \gg g\mu_B B_{||}/\hbar$ ). (C) Spin relaxation data for the same single shallow-implant NV before silver deposition (open blue squares), with silver deposited (red circles) and after the silver has been removed (open blue triangles). (D) Spin relaxation for a single NV close to a silver film prepared in the  $|m_s = 0\rangle$  state (red circles) and in the  $|m_s = -1\rangle$  state (open orange circles). (Inset) Spin relaxation for a single native NV in bulk diamond in the  $|m_s = 0\rangle$  state (blue circles) and in the  $|m_s = -1\rangle$  state (open light blue circles).

<sup>1</sup>Department of Physics, Harvard University, Cambridge, MA 02138, USA. <sup>2</sup>Department of Chemistry and Chemical Biology, Harvard University, Cambridge, MA 02138, USA. <sup>3</sup>Department of Physics, University of Maryland, College Park, MD 20742, USA.

\*These authors contributed equally to this work. †Corresponding author. E-mail: lukin@physics.harvard.edu (M.D.L.); hongkun\_park@harvard.edu (H.P.)

in the absence of external noise, the spin lifetime is limited by phonon-induced relaxation to  $T_1^{\text{ph}} \approx 4$  ms. With the silver nearby, the lifetime of the  $|m_s = 0\rangle$  state is reduced to  $T_1 = 165$   $\mu\text{s}$ , which we attribute to magnetic Johnson noise emanating from the film. To verify that the enhanced relaxation is due to magnetic noise, we compare the lifetime of the  $|m_s = 0\rangle$  state, which has magnetic dipole allowed transitions to both of the  $|m_s = \pm 1\rangle$  states, to that of the  $|m_s = -1\rangle$  state, which can only decay directly to the  $|m_s = 0\rangle$  state (Fig. 1D). As expected for relaxation induced by magnetic noise, the  $|m_s = -1\rangle$  state has approximately twice the lifetime of the  $|m_s = 0\rangle$  state (23). This is in contrast to the observed lifetimes when limited by phonon-induced relaxation (Fig. 1D, inset), where the  $|m_s = 0\rangle$  and  $|m_s = \pm 1\rangle$  states have almost identical lifetimes (24). In what follows, we define  $T_1$  as the lifetime of the  $|m_s = 0\rangle$  state.

To test the scaling of Johnson noise with distance ( $d$ ) to the metal, we deposit a layer of  $\text{SiO}_2$  on the diamond surface with a gradually increasing thickness (Fig. 2A). We characterize the thickness of the  $\text{SiO}_2$  layer as a function of position on the sample (Fig. 2B, inset) and deposit a 60-nm polycrystalline silver film on top of the  $\text{SiO}_2$ . The conductivity of the silver film is measured to be  $2.9 \times 10^7$  S/m at room temperature. By measuring the relaxation rates  $\Gamma = 1/T_1$  of individual NVs at different positions along the  $\text{SiO}_2$  ramp, we extract the distance dependence of the noise (Fig. 2B), with the uncertainty in the distance dominated by the variation in the implanted depth of the NVs (taken to be  $15 \pm 10$  nm). To ensure that the measured rates are Johnson noise limited, we measure the spin relaxation of 5 to 10 randomly selected NVs per location along the ramp and plot the minimum observed rate at each location (23). As expected (7–9), the magnitude of the noise increases as the NVs approach the silver surface.

To investigate the dependence of the noise on temperature and conductivity, we deposit a 100-nm polycrystalline silver film on a diamond sample and measure the  $T_1$  of a single NV beneath the silver over a range of temperatures ( $\sim 10$  to 295 K). The measured relaxation rate for a single NV near the silver increases with temperature (red circles in Fig. 3A), as expected for thermal noise, but the scaling is clearly nonlinear. This can be understood by recognizing that the conductivity of the silver film is also a function of temperature and that the magnitude of the thermal currents in the silver depends on the conductivity. To account for this effect, a four-point resistance measurement of the silver film is performed to determine the temperature dependence of the bulk conductivity of the silver film (Fig. 3B).

To analyze the dependence of the NV spin relaxation rate on distance, temperature, and conductivity, we use the model of (6), in which an electronic spin-1/2 qubit with Larmor frequency  $\omega_L$  is positioned at a distance  $d$  from the surface of a metal. For silver at room temperature,

the skin depth at  $\omega_L$  is  $\delta \approx 1$   $\mu\text{m}$ ; consequently, when  $d < 100$  nm, we are in the “quasi-static” limit  $d \ll \delta$ . The thermal limit  $k_B T \gg \hbar \omega_L$  is valid for all temperatures in this work. In this regime, the magnetic noise spectral density perpendicular to the silver surface is given by

$$S_B^z = \frac{\mu_0^2 k_B T \sigma}{16\pi d} \quad (1)$$

where  $\sigma$  is the temperature-dependent conductivity of the metal as defined by the Drude model. This scaling can be intuitively understood by considering the magnetic field generated by a single thermal electron in the metal at the NV position,  $B_0 = \frac{\mu_0 e v_{\text{th}}}{4\pi d^2}$ , where the thermal velocity  $v_{\text{th}} \propto \sqrt{k_B T/m_e}$ ,  $m_e$  is the effective mass of electrons in silver, and  $e$  is the electron charge. In the limit  $d \ll \delta$ , screening can be safely ignored, and the NV experiences the magnetic field

spectrum arising from  $N$  independent electrons in a volume  $V$ ;  $S_B \propto V n(B_0)^2 \tau_c$ , where  $n$  is the electron density and  $\tau_c$  is the correlation time of the noise, given by the average time between electron scattering events; and  $\tau_c = l/v_F$ , where  $l$  is the electron mean free path and  $v_F$  is the Fermi velocity. Recognizing that the NV is sensitive to the motion of electrons within a sensing volume  $V \propto d^3$ , we arrive at the scaling given by Eq. 1, with  $\sigma = \frac{ne^2 \tau_c}{m_e}$ . Applying Fermi's golden rule and accounting for the orientation and spin-1 of the NV yields the relaxation rate for the  $|m_s = 0\rangle$  state

$$\Gamma = \frac{1}{T_1} = \frac{3g^2 \mu_B^2}{2\hbar^2} S_B^z \left(1 + \frac{1}{2} \sin^2(\theta)\right) \quad (2)$$

where  $g \approx 2$  is the electron  $g$ -factor,  $\mu_B$  is the Bohr magneton, and  $\theta \approx 54.7^\circ$  is the angle of the

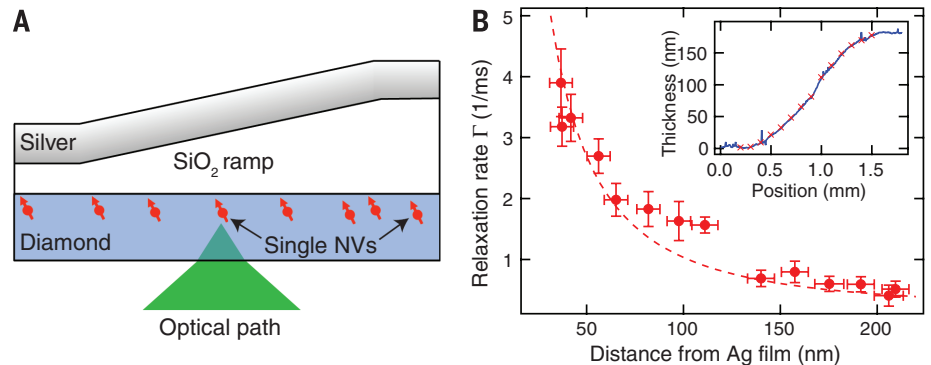


**Fig. 2. Distance dependence of NV relaxation close to silver.** (A) A gradual  $\text{SiO}_2$  ramp (slope of  $\sim 0.2$  nm/ $\mu\text{m}$ ) is grown on the diamond surface, followed by a 60-nm silver film. (B) The NV relaxation rate is measured as a function of position along the ramp, which is then converted to distance to the film. At each point, 5 to 10 NV centers are measured, and the minimum rate measured is plotted (red circles). The horizontal error bars reflect 1 SD in the estimated distance to the film including the uncertainty in NV depth, while the vertical error bars reflect 1 SD in the fitted relaxation rate. The red dashed line shows the expected relaxation rate with no free parameters after accounting for the finite silver film thickness. (Inset) Thickness of the ramp as a function of lateral position along the diamond sample (blue curve). The red crosses correspond to the positions along the sample where the measurements were taken.

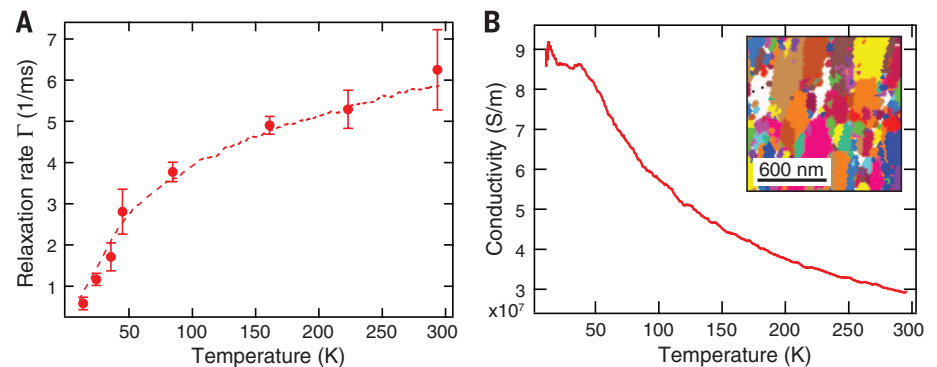


**Fig. 3. Temperature dependence of NV relaxation close to polycrystalline silver.** (A) The measured relaxation rate of a single NV spin under a polycrystalline silver film as a function of temperature (red data points). The error bars reflect 1 SD in the fitted relaxation rate. The conductivity of the silver film as a function of temperature shown in (B) is included in a fit to Eq. 2, with the distance to the film as the single free parameter (red dashed line). The extracted distance is  $31 \pm 1$  nm. (B) The conductivity of the 100-nm-thick polycrystalline silver film deposited on the diamond surface is measured as a function of temperature. (Inset) Grain boundaries within the polycrystalline silver film, imaged using electron backscatter diffraction. The average grain diameter is 140 nm, with a SD of 80 nm.

NV dipole relative to the surface normal vector (23). In Fig. 2B, the inverse scaling with distance  $d$  predicted by Eq. 1 is clearly evident for NVs very close to the silver. At distances comparable to the silver film thickness, Eq. 1 is no longer valid, but we recover excellent agreement with the no-free-parameters prediction of Eq. 2 by including a correction for the thickness of the silver film (red dashed line in Fig. 2B), which is measured independently. The measured relaxation rates as a function of temperature are also in excellent agreement with the predictions of Eq. 2 (red dashed line in Fig. 3A), while the extracted distance of  $31 \pm 1$  nm is consistent with the expected depth (23).

Notably, very different results are obtained when we replace the polycrystalline film with single-crystal silver. For this experiment, a 1.5- $\mu\text{m}$ -thick single-crystal silver film grown by sputtering onto silicon (23, 25, 26) is placed in contact with the diamond surface. The measured conductivity of the single-crystal silver exhibits a much stronger temperature dependence (blue line in Fig. 4A) as compared to that of the 100-nm-thick polycrystalline film. Figure 4B

presents the measured relaxation rate as a function of temperature for an NV in a region in direct contact with the single-crystal silver (blue squares). The dashed blue line corresponds to the temperature-dependent rate predicted by Eq. 2, which strongly disagrees with the experimental results. Specifically, because the measured silver conductivity increases faster than the temperature decreases in the range from room temperature down to 40 K, Eq. 2 predicts that the relaxation rate should increase as the temperature drops, peaking at 40 K and then dropping linearly with temperature once the conductivity saturates. Instead, the  $T_1$  of the NV consistently increases as the temperature drops, implying that at lower temperatures, the silver produces considerably less noise than expected from Eq. 2. We observe similar deviation from the prediction of Eq. 2 for all 23 NVs measured in the vicinity of the single-crystal silver (23).

To analyze these observations, we note that the conventional theoretical approach (6) resulting in Eq. 2 treats the motion of the electrons in the metal as entirely diffusive, using Ohm's law,

$\mathbf{J}(\mathbf{r}, t) = \sigma \mathbf{E}(\mathbf{r}, t)$ , to associate the bulk conductivity of the metal with the magnitude of the thermal currents. While accurately describing the observed relaxation rates next to the polycrystalline material, where the resistivity of the film is dominated by electron scattering off grain boundaries (Fig. 3B, inset), this assumption is invalid in the single-crystal silver film experiments, particularly at low temperatures. Here, the measured conductivity of the single-crystal film indicates that the mean free path  $l$  is greater than 1  $\mu\text{m}$ , considerably exceeding the sensing region determined by the NV-metal separation, and thus the ballistic motion of the electrons must be accounted for. Qualitatively, the correlation time of the magnetic noise in this regime is determined by the ballistic time of flight of electrons through the relevant interaction region  $\tau_c \sim d/v_F$  (Fig. 4C). This results in a saturation of the noise spectral density and the spin relaxation rate  $\Gamma$  as either the NV approaches the silver surface or the mean free path becomes longer at lower temperatures (23), with the ultimate limit to the noise spectrum given by:

$$S_B^z = \frac{2 \mu_0^2 k_B T}{\pi} \frac{ne^2}{m_e v_F} \quad (3)$$

This regime of magnetic Johnson noise was recently analyzed theoretically (11) using the Lindhard form nonlocal dielectric function for the metal modified for finite electron scattering times (23, 27, 28). Comparison of this model (solid line in Fig. 4B) to the data, with distance again as the only free parameter, yields excellent agreement for all 23 measured NVs (23). Figure 4D shows the measured  $T_1$  times at 103 and 27 K for each NV as a function of extracted distance (blue triangles). Of the 23 NVs measured, 15 are in a region of the diamond sample in direct contact with the silver (23). Excellent agreement between the nonlocal model (solid lines) and the data is observed for all 23 NVs at all 12 measured temperatures. Apparent in Fig. 4D is the saturation of the relaxation rate as the NV approaches the silver surface and as the mean free path becomes longer at lower temperatures (dashed black line), as predicted by Eq. 3.

Although ballistic electron motion in nanoscale structures has previously been studied and utilized (12, 13), our approach allows for non-invasive probing of this and related phenomena and provides the possibility for studying mesoscopic physics in macroscopic samples. The combination of sensitivity and spatial resolution demonstrated here enables direct probing of current fluctuations in the proximity of individual impurities, with potential applications such as imaging of Kondo states and probing of novel two-dimensional materials (29), where our technique may allow for the spatially resolved probing of edge states (12). Likewise, it could enable investigation of the origin of  $1/f$  flux noise by probing magnetic fluctuations near superconducting Josephson circuits (30, 31). Finally, as Johnson noise presents an important limitation to the control of classical and quantum mechanical devices at small length scales (6–10), the present

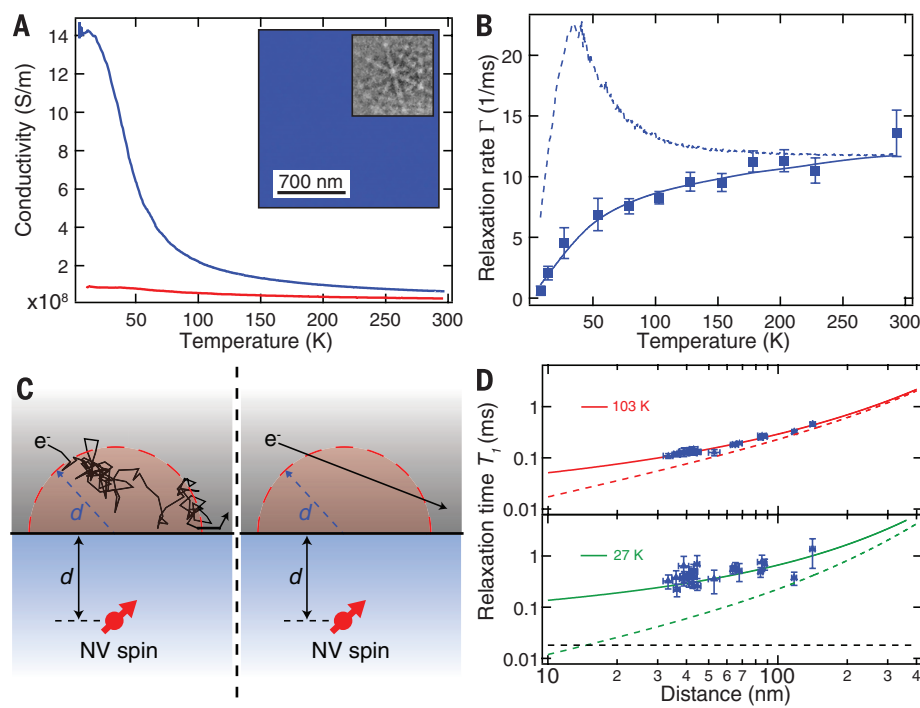


**Fig. 4. Temperature dependence of NV relaxation close to single-crystal silver.** (A) Measured conductivity of single-crystal (blue curve) and polycrystalline (red curve, same as Fig. 3B) silver as a function of temperature. (Inset) Electron backscatter diffraction image of the single-crystal silver film showing no grain boundaries, and the observed diffraction pattern. (B) Relaxation of a single NV spin under single-crystal silver as a function of temperature (blue squares). The error bars reflect 1 SD in the fitted relaxation rate. Equation 2 is fit to the data from 200 to 295 K (blue dashed line). A nonlocal model (23) is fit to the data (blue solid line); the extracted distance between the NV and the silver surface is  $36 \pm 1$  nm. (C) Cartoon illustrating the relevant limits, where the noise is dominated by diffusive electron motion (left,  $l \ll d$ ) and ballistic motion (right,  $l \gg d$ ). (D) The same data as in (B) were taken for 23 NVs at varying distances from the film. The  $T_1$  of each NV at 103 K (top) and 27 K (bottom) is plotted against the extracted depth (blue triangles). The horizontal error bars reflect 1 SD in the fitted distance to the film, while the vertical error bars reflect 1 SD in the fitted relaxation time. The nonlocal model (solid colored lines) saturates at a finite lifetime determined by Eq. 3 (bottom, dashed black line), whereas the local model does not (dashed colored lines).



results demonstrate that this limitation can be circumvented by operating below the length scale determined by the electron mean free path.

## REFERENCES AND NOTES

1. M. Lundström, *Science* **299**, 210–211 (2003).
2. B. Weber *et al.*, *Science* **335**, 64–67 (2012).
3. Q. Xu, B. Schmidt, S. Pradhan, M. Lipson, *Nature* **435**, 325–327 (2005).
4. L. Novotny, B. Hecht, *Principles of Nano-optics* (Cambridge Univ. Press, Cambridge, 2012).
5. A. L. Falk *et al.*, *Nat. Phys.* **5**, 475–479 (2009).
6. C. Henkel, S. Pötting, M. Wilkens, *Appl. Phys. B* **69**, 379–387 (1999).
7. Y. J. Lin, I. Teper, C. Chin, V. Vuletić, *Phys. Rev. Lett.* **92**, 050404 (2004).
8. M. P. A. Jones, C. J. Vale, D. Sahagun, B. V. Hall, E. A. Hinds, *Phys. Rev. Lett.* **91**, 080401 (2003).
9. D. Harber, J. McGuirk, J. Obrecht, E. Cornell, *J. Low Temp. Phys.* **133**, 229–238 (2003).
10. M. Brownnutt, M. Kumph, P. Rabl, R. Blatt, <http://arxiv.org/abs/1409.6572> (2014).
11. L. S. Langsjoen, A. Poudel, M. G. Vavilov, R. Joynt, *Phys. Rev. A* **86**, 010301 (2012).
12. C. Beenakker, H. van Houten, *Solid State Phys.* **44**, 1–228 (1991).
13. S. Datta, *Electronic Transport in Mesoscopic Systems* (Cambridge Univ. Press, Cambridge, 1997).
14. A. C. Bleszynski-Jayich *et al.*, *Science* **326**, 272–275 (2009).
15. H. Bluhm, N. C. Koshnick, J. A. Bert, M. E. Huber, K. A. Moler, *Phys. Rev. Lett.* **102**, 136802 (2009).
16. D. Rothfuß, A. Reiser, A. Fleischmann, C. Enss, *Appl. Phys. Lett.* **103**, 052605 (2013).
17. L. Childress *et al.*, *Science* **314**, 281–285 (2006).
18. J. R. Maze *et al.*, *Nature* **455**, 644–647 (2008).
19. G. Balasubramanian *et al.*, *Nature* **455**, 648–651 (2008).
20. J. P. Tetienne *et al.*, *Science* **344**, 1366–1369 (2014).
21. E. Schäfer-Nolte, L. Schlupf, M. Ternes, F. Reinhard, K. Kern, J. Wrachtrup, <http://arxiv.org/abs/1406.0362> (2014).
22. M. Pelliccione, B. A. Myers, L. Pascal, A. Das, A. C. Bleszynski Jayich, <http://arxiv.org/abs/1409.2422> (2014).
23. Materials and methods are available as supporting material on Science Online.
24. T. H. Taminiau, J. Cramer, T. van der Sar, V. V. Dobrovitski, R. Hanson, *Nat. Nanotechnol.* **9**, 171–176 (2014).
25. A. A. Baski, H. Fuchs, *Surf. Sci.* **313**, 275–288 (1994).
26. J. H. Park *et al.*, *Adv. Mater.* **24**, 3988–3992 (2012).
27. G. W. Ford, W. Weber, *Phys. Rep.* **113**, 195–287 (1984).
28. N. W. Ashcroft, N. D. Mermin, *Solid State Physics* (Holt, Rinehart and Winston, New York, 1976).
29. P. Maher *et al.*, *Science* **345**, 61–64 (2014).
30. L. Faoro, L. B. Ioffe, *Phys. Rev. Lett.* **100**, 227005 (2008).
31. S. M. Anton *et al.*, *Phys. Rev. Lett.* **110**, 147002 (2013).

## ACKNOWLEDGMENTS

We thank E. Demler, A. Bleszynski Jayich, B. Myers, A. Yacoby, M. Vavilov, R. Joynt, A. Poudel, and L. Langsjoen for helpful discussions and insightful comments. Financial support was provided by the Center for Ultracold Atoms, the National Science Foundation (NSF), the Defense Advanced Research Projects Agency Quantum-Assisted Sensing and Readout program, the Air Force Office of Scientific Research Multidisciplinary University Research Initiative, and the Gordon and Betty Moore Foundation. S.K. and A.S. acknowledge financial support from the National Defense Science and Engineering Graduate fellowship, V.E.M. from the Society of Fellows of Harvard University, and S.K. from the NSF Graduate Research Fellowship. All fabrication and metrology were performed at the Center for Nanoscale Systems (CNS), a member of the National Nanotechnology Infrastructure Network, which is supported by the NSF under award no. ECS-0335765. The CNS is part of Harvard University.

## SUPPLEMENTARY MATERIALS

[www.sciencemag.org/content/347/6226/1129/suppl/DC1](http://www.sciencemag.org/content/347/6226/1129/suppl/DC1)  
Materials and Methods  
Figs. S1 to S7  
Tables S1 to S3  
References (32–34)

4 December 2014; accepted 16 January 2015  
Published online 29 January 2015;  
10.1126/science.aaa4298

## REPELLENT MATERIALS

# Robust self-cleaning surfaces that function when exposed to either air or oil

Yao Lu,<sup>1</sup> Sanjayan Sathasivam,<sup>1</sup> Jinlong Song,<sup>2</sup> Colin R. Crick,<sup>3</sup>  
Claire J. Carmalt,<sup>1</sup> Ivan P. Parkin<sup>1\*</sup>

Superhydrophobic self-cleaning surfaces are based on the surface micro/nanomorphologies; however, such surfaces are mechanically weak and stop functioning when exposed to oil. We have created an ethanolic suspension of perfluorosilane-coated titanium dioxide nanoparticles that forms a paint that can be sprayed, dipped, or extruded onto both hard and soft materials to create a self-cleaning surface that functions even upon emersion in oil. Commercial adhesives were used to bond the paint to various substrates and promote robustness. These surfaces maintained their water repellency after finger-wipe, knife-scratch, and even 40 abrasion cycles with sandpaper. The formulations developed can be used on clothes, paper, glass, and steel for a myriad of self-cleaning applications.

Artificial self-cleaning surfaces work through extreme water repellence (superhydrophobicity) so that water forms near spherical shapes that roll on the surface; the rolling motion picks up and removes dirt, viruses, and bacteria (1–3). To achieve near spherical water droplets, the surfaces must be highly textured (rough) combined with extremely low water affinity (waxy) (4, 5). The big drawback of these artificial surfaces is that they are readily abraded (6–8), sometimes with little more than brushing with a tissue, and readily contaminated by oil (9–11). We report here a facile method for making superhydrophobic surfaces from both soft (cotton or paper) and hard (metal or glass) materials. The process uses dual-scale nanoparticles of titanium dioxide (TiO<sub>2</sub>) that are coated with perfluorooctyltriethoxysilane. We created an ethanol-based suspension that can be sprayed, dipped, or painted onto surfaces to create a resilient water-repellent surface. By combining the paint and adhesives, we created a superhydrophobic surface that showed resilience and maintained its performance after various types of damage, including finger-wipe, knife-scratch, and multiple abrasion cycles with sandpaper. This method can also be used for components that require self-cleaning and lubricating such as bearings and gears, to which superamphiphobic (repels oil and water) surfaces (9–11) are not applicable.

A paint was created by mixing two different size ranges of TiO<sub>2</sub> nanoparticles (~60 to 200 nm and ~21 nm) in an ethanol solution containing perfluorooctyltriethoxysilane (12). Scanning electron microscopy (SEM) and transmission electron microscopy (TEM) of the constituent particles

of the paint (Fig. 1A) show the dual-scale nature of the TiO<sub>2</sub> nanoparticles. X-ray photoelectron spectroscopy (XPS) (Fig. 1B) showed that the titanium dioxide particles were coated with perfluorooctyltriethoxysilane.

We used many different coating methods to create the water-repellent surfaces, including an artist's spray-gun to coat hard substrates such as glass and steel, dip-coating for cotton wool, and a syringe (movie S1) to extrude the paint onto filter paper. After allowing the ethanol to evaporate for ~180 s at room temperature, the treated areas of the substrates supported water as near spherical droplets, whereas the untreated parts were readily wetted (it required ~30 min for the ethanol to fully evaporate from cotton wool and filter paper at room temperature) (fig. S1). We used x-ray diffraction (XRD) (Fig. 1C) to analyze the coatings on hard and soft substrates. The diffraction peaks show the expected patterns for nanoscaled TiO<sub>2</sub>.

On a surface that shows water repellence, water droplets tend to bounce instead of wetting the surface (13, 14). However, for soft substrates, extreme superhydrophobicity is required to achieve the bouncing phenomenon because the water droplets tend to be trapped onto the threads of the substrates (cotton wool) (15). Shown in fig. S2 are the water dropping tests on untreated glass, steel, cotton wool, and filter paper, which were readily wetted (the contact moment of the water droplets and the solid surfaces is defined as 0). Shown in Fig. 2 is the water bouncing process on dip-coated glass, steel, cotton wool, and filter paper surfaces. Water droplets completely leave the surface without wetting or even contaminating the surfaces (the water was dyed blue to aid visualization), indicating that the surfaces were superhydrophobic. In movie S2, we compare the water-affecting behavior between untreated and treated glass, steel, cotton wool, and filter paper, respectively. The effect of artificial rain on the treated surfaces is shown in movie S3; the drop sizes varied with random impact

<sup>1</sup>Department of Chemistry, University College London, 20 Gordon Street, London, WC1H 0AJ, UK. <sup>2</sup>Key Laboratory for Precision and Non-traditional Machining Technology of Ministry of Education, Dalian University of Technology, Dalian, 116024, People's Republic of China. <sup>3</sup>Department of Chemistry, Imperial College London, South Kensington Campus, London, SW7 2AZ, UK.

\*Corresponding author. E-mail: [i.p.parkin@ucl.ac.uk](mailto:i.p.parkin@ucl.ac.uk)

---

*This copy is for your personal, non-commercial use only.*

---

**If you wish to distribute this article to others**, you can order high-quality copies for your colleagues, clients, or customers by [clicking here](#).

**Permission to republish or repurpose articles or portions of articles** can be obtained by following the guidelines [here](#).

**The following resources related to this article are available online at [www.sciencemag.org](http://www.sciencemag.org) (this information is current as of June 25, 2015 ):**

**Updated information and services**, including high-resolution figures, can be found in the online version of this article at:

<http://www.sciencemag.org/content/347/6226/1129.full.html>

**Supporting Online Material** can be found at:

<http://www.sciencemag.org/content/suppl/2015/01/28/science.aaa4298.DC1.html>

A list of selected additional articles on the Science Web sites **related to this article** can be found at:

<http://www.sciencemag.org/content/347/6226/1129.full.html#related>

This article **cites 27 articles**, 6 of which can be accessed free:

<http://www.sciencemag.org/content/347/6226/1129.full.html#ref-list-1>

This article has been **cited by** 1 articles hosted by HighWire Press; see:

<http://www.sciencemag.org/content/347/6226/1129.full.html#related-urls>

This article appears in the following **subject collections**:

Materials Science

[http://www.sciencemag.org/cgi/collection/mat\\_sci](http://www.sciencemag.org/cgi/collection/mat_sci)